PIV measurement of mildly controlled flow over a straight-wing model

Pramod Salunkhe[1], Hui Tang[2*], Yingying Zheng[3], Yanhua Wu[3]

[1]Department of Mechanical Engineering, Dr. D.Y. Patil Institute of Engineering, Management & Research, Akurdi, Pune – 411 045, Maharashtra, India

[2]Department of Mechanical Engineering, The Hong Kong Polytechnic University, Kowloon, Hong Kong SAR, China

[3]School of Mechanical & Aerospace Engineering, Nanyang Technological University, Singapore 639798

[*]Corresponding author: Tel.: +852-27667815; Fax: +852-23654703; Email: h.tang@polyu.edu.hk

Abstract:

This paper follows our previous work [Tang et al. *Exp. Therm. Fluid Sci.* 57:1-10 (2014)] to further demonstrate the effectiveness of a newly developed synthetic-jet (SJ) array in flow separation control over a straight-wing model using tomographic particle image velocimetry (Tomo-PIV) measurements. The wing model is tested in a wind tunnel at a fixed angle of attack 19° and chord Reynolds number 1.2×10^5, with the SJ array operating with a momentum coefficient of 4.2×10^{-5} and a reduced frequency of 7.2. Different from all existing SJ-based flow separation control, the present control is so mild that the controlled flow sometimes attaches to and sometimes separates from the wing surface. Both time-averaged and phase-locked flow fields are presented and analyzed. It is found that the control effect reaches its maximum at the nominal phase angle 180°, which is close to the instant when the SJ array achieves its maximum blowing. Significant reduction of the shape factor confirms the effectiveness of the current SJ array in overcoming flow separation. The proper orthogonal decomposition (POD) analysis reveals that, no matter whether the SJ array is actuated or not, the first mode consists of a 2D plane jet-like flow over the wing surface, carrying more than 70% of the total fluctuation energy. Although not strong enough to change this dominant mode, the present mild SJ control significantly increases the occurrence rate of flow attachment. The conditional turbulent kinematic energy (TKE) is also analyzed. It is found that while the introduction of the SJs has little influence on the conditional TKE for the separated flows, it reduces the thickness of the wall-attached layer of high TKE values for the attached flows.

Nomenclature:

A	actuator orifice area, m^2
b	wing span, m
c	wing chord, m
C_μ	momentum coefficient
f	actuation frequency, Hz
F^+	reduced frequency
H	shape factor
k	turbulent kinetic energy, m^2/s^2
n	number of actuators in an array
N	number of snapshots
q	POD temporal coefficient
U_j	averaged synthetic jet velocity, m/s
U_∞	free-stream velocity, m/s
$\bar{u}$	mean streamwise flow velocity, m/s
$u^{'}$	fluctuating streamwise velocity, m/s
$v^{'}$	fluctuating wall-normal velocity, m/s
$w^{'}$	fluctuating spanwise velocity, m/s

Greek Symbols:

λ	eigenvalue
λ_{ci}	local swirl strength, 1/s
Φ	spatial POD mode

1 Introduction

Synthetic jet (SJ), also known as a zero-net-mass-flux jet, provides a novel means of flow control due to its ability of injecting non-zero momentum into external flow with zero net mass flux (Smith & Glezer 1998; Amitay et al. 2001; Amitay & Glezer 2002; Zhong et al. 2007; Zhong & Zhang 2013). A typical SJ actuator consists of a cavity with an oscillatory diaphragm on its bottom side and an orifice on the opposite. The diaphragm's periodic downward and upward motion generates a succession of

vortex rings/pairs that propagate away from the orifice/slot, synthesizing a SJ. Since emerging in 1990s, its capability in flow separation control has been well demonstrated in many lab experiments (Mccormick 2000; Crook & Wood 2001; Melton et al. 2004; Ciuryla et al. 2007).

The effectiveness of SJ-based flow separation control depends very much on the SJ strength and frequency. Lee et al. (2003) mentioned that the SJ strength must be sufficiently high to ensure effective flow control, and they used a blowing ratio close to one in their control. Glezer & Amitay (2002) provided an in-depth review on interaction between SJs and separated flows, and suggested that the SJ actuation frequency should be at least an order of magnitude higher than the natural shedding frequency of an airfoil for effective flow control. However, recently Franck & Colonius (2012) reported that low-frequency actuation at the order of natural shedding frequency of a hump model was more effective in reducing the flow separation than high-frequency actuation.

The application of SJs on airfoils has been reported in many works. For instance, You and Moin (2008) evaluated the effectiveness of a SJ over a NACA 0015 airfoil, and showed that the introduction of SJ led to an improvement in lift coefficient by about 70%. They concluded that the SJ not only adds momentum to the boundary layer flow but also enhances mixing between the primary and boundary layer flows. Wood et al. (2009) performed PIV measurements over a NACA 4421 wing model and observed that counter-rotating vortical structures lose their strength and lift off the wing surface as they propagate downstream. They reported that the 2D vortices near the jet orifice break down to 3D flow structures as they move downstream that improves mixing between the primary and boundary layer flows.

Different from most of existing SJ-based flow separation control where strong enough SJs (momentum coefficient $C_\mu > 10^{-4}$) were used, the present study aims to unveil more flow details of mildly controlled separated flow over a straight-wing model using a newly developed SJ array. The SJ array used in the control produces SJs with a relatively smaller momentum coefficient ($C_\mu = 4.2 \times 10^{-5}$ at SJ actuation frequency 400 Hz). In addition to the hot-wire and force measurement results released in our previous work (Tang et al. 2014), a key portion of the flow over the wing's suction surface with and without the SJ control is measured using a tomographic particle image velocimetry (Tomo-PIV) system. Both time-averaged and phase-locked PIV results are presented and analyzed to show the effect of this control. Two advanced flow analysis methods, i.e., the proper orthogonal decomposition

(POD) analysis and the analysis of conditional turbulent quantities, are applied to the three-dimensional PIV data to reveal meaningful difference between the flow fields with and without the SJ control.

This paper is organized as follows. The SJ array and experimental test rig are briefly introduced in Section 2. New results are presented and discussed in Section 3, including the time-averaged and phase-locked velocity and vortex fields, the POD modes and coefficient distribution and the conditional turbulent kinetic energy for the separated and attached flows. In the end, conclusions are drawn in Section 4.

2 SJ array design and experimental test rig

Experiments were carried out on a low speed straight-wing model, LS(1)-0421MOD, in a subsonic wind tunnel of test section size, 0.8 m (W) × 0.8 m (H) × 2 m (L). The wing model has a chord length of 180 mm and a span of 255 mm. In the present work, a SJ array is used as a means of active flow control over the suction surface of the wing model. The SJ actuator comprises of four 20 mm diameter piezoelectric diaphragms attached on its four sidewalls as shown in Fig. 1. Multiple such actuators are arrayed and incorporated inside the wing model. An orifice of the SJ actuator comprises of five 1-mm-diameter holes in a row on the wing model, with a center-to-center distance of 2 mm between the successive holes. An array of such ten SJ actuators is located at 23% of the chord. The SJ array is excited in phase using two power amplifiers, which are interfaced with a function generator to generate a sinusoidal waveform at various voltages and frequencies. All the experiments were carried out at an actuation frequency of 400 Hz and excitation voltage of 200 V. In the present study, a nominal phase angle of the SJ array is defined based on the output signal from the function generator, with the crest at phase angle 90° and the trough at 270°.
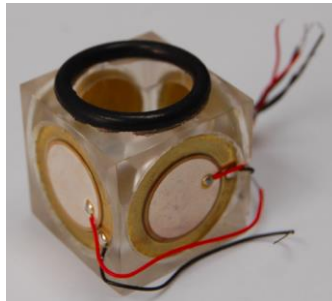

Fig. 1 A single SJ actuator

A three-dimensional Tomo-PIV system was used to capture the flow-field, as shown in Figure 2(a). The Tomo-PIV setup is similar to the one adopted in our past studies (Lee & Wu 2013a, 2013b, 2015)

and more PIV details can be found in them. A pair of high energy (~450 mJ/pulse) Nd:YAG laser was used to illuminate the flow over the wing model suction surface to produce a laser volume sheet of 7 mm thickness. The laser volume sheet was aligned in such a way that it covers a half of the second SJ actuator in the array, with its left edge right across the center of the third hole and its right edge falling between two neighboring actuators. The location of the laser volume sheet relative to the SJ orifice is shown in Fig. 2(b).
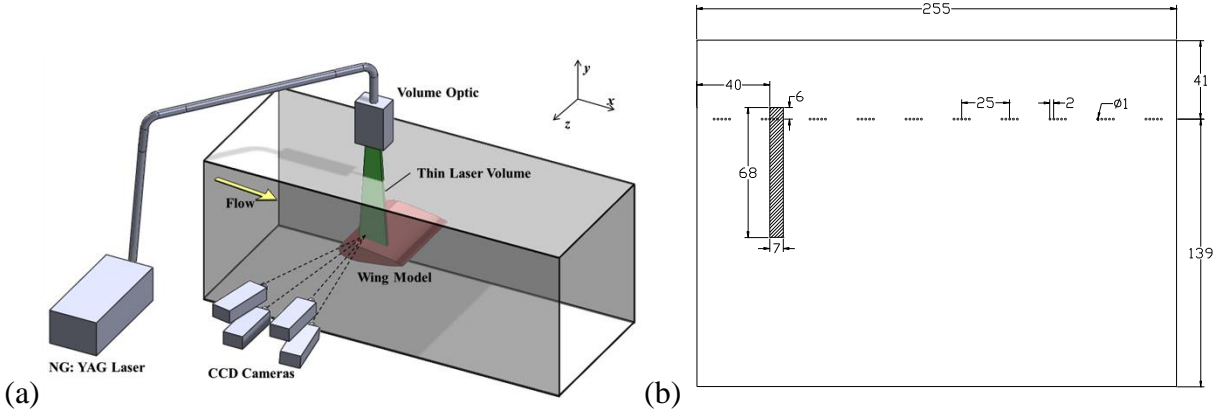

Fig. 2 (a) Experimental setup of Tomo-PIV measurements (b) plan view of the laser volume on wing surface

A Laskin nozzle (Oil Droplet Generator 9307 from TSI) was used to generate the seeding particles of 1-2 µm size. The seeding flow was captured using four 16-bit CCD cameras with a focal length of 105 mm. Each camera has a resolution of 2456 x 2058 pixels with a pixel size of 3.45 µm. The laser volume sheet size of 68 mm (x) $\times$ 56 mm (y) $\times$ 7 mm (z) results in velocity vector field of 106 (x) $\times$ 88 (y) $\times$ 12 (z) with a grid spacing of 0.64 mm. The three-dimensional light intensity field is reconstructed using FastMART algorithm. Subsequently, the three-dimensional velocity vector field is obtained using the three-dimensional particle pattern cross-correlation of reconstructed particle distribution. A modified median filter is used to remove the spurious vectors in the velocity vector field. About 2% bad velocity vectors were removed and then filled through interpolation. Subsequently, the velocity vector field is low pass filtered to remove any noise associated with the higher frequencies. To enable phase-locked PIV measurements at different phase angles, the amplifier output signal and the laser trigger signal were shown in a digital oscilloscope. Suitable values for time delay were set in a digital delay generator to generate the required phase angles. In the present study, the phase-locked PIV measurements were carried out at eight different phase angles, namely, 0°, 45°, 90°, 135°, 180°, 225°,

270° and 315°. At each phase angle, 200 pairs of seeding particle images were recorded by each of the four CCD cameras.

The uncertainty in PIV measurement was found to be 0.1 voxel for both streamwise and normal velocity components and 0.15 voxel for spanwise velocity component. These uncertainties were determined based on the earlier studies of Elsinga et al. (2006) and Scarano and Poelma (2009).

In the present study, all the PIV measurements were carried out at a constant wind speed $U_\infty = 10$ m/s and a fixed angle of attack 19°. The corresponding chord Reynolds number is 1.2×10^5. The SJ array was operated at 200 V excitation voltage and 400 Hz frequency that is close to the actuator's Helmholtz frequency. At this condition, previous hot-wire anemometer measurements revealed that the peak SJ velocity is about 7 m/s. The corresponding jet-to-free-stream velocity ratio is 0.22 (calculated using the SJ mean blowing velocity U_j) in the presence of cross-stream flow, the corresponding momentum coefficient is about 4.2×10^{-5} based on the formula $C_\mu = nAU_j^2/bcU_\infty^2$, and the reduced frequency (F^+) is 7.2 based on the formula $F^+ = fc/U_\infty$. Previous force measurements revealed that at 400 Hz actuation frequency, the largest improvement in lift coefficient and average reduction in drag coefficient are 22.6% and 17.1%, respectively. More detailed results about the force-balance measurements can be found in Tang et al. (2014).

3 Results and Discussion

3.1. Velocity and vortex fields

With the obtained Tomo-PIV data, the velocity and vortex fields with and without the SJ actuation can be investigated both qualitatively and quantitatively. Figure 3 shows 3D vortex structures colored by streamwise velocity, with velocity vectors and contours illustrated in the background, for the time-averaged baseline case, time-averaged SJ actuation case and various phase-locked SJ actuation cases. These vortex structures are identified using iso-surfaces of local swirling strength λ_{ci}, the imaginary part of the complex eigenvalue pair of local velocity gradient (Zhou et al. 1999). A relatively high λ_{ci} value is chosen in order to show the dominant vortex structures clearly. From Fig. 3, it can be seen that most of the vortex structures fall within the shear layer that splits the flow field into two distinct flow regions, namely, the free-stream flow region and the near-wall retarding flow region. The baseline case shows substantial congestion of large-size vortex structures in the shear layer. After switching on the SJ array, significant alteration in the flow field can be observed as evident in the time-averaged and eight

phase-averaged vortex/velocity fields. By comparing the two time-averaged flow fields, the cumulative effects of the SJ actuation are observed as described in Tang et al. (2014): (i) the congested, continuous large vortex structures are broken down and shrink significantly; (ii) the vortex trajectory is brought down towards the wing surface; and (iii) the near-wall flow is re-energized to overcome flow separation.
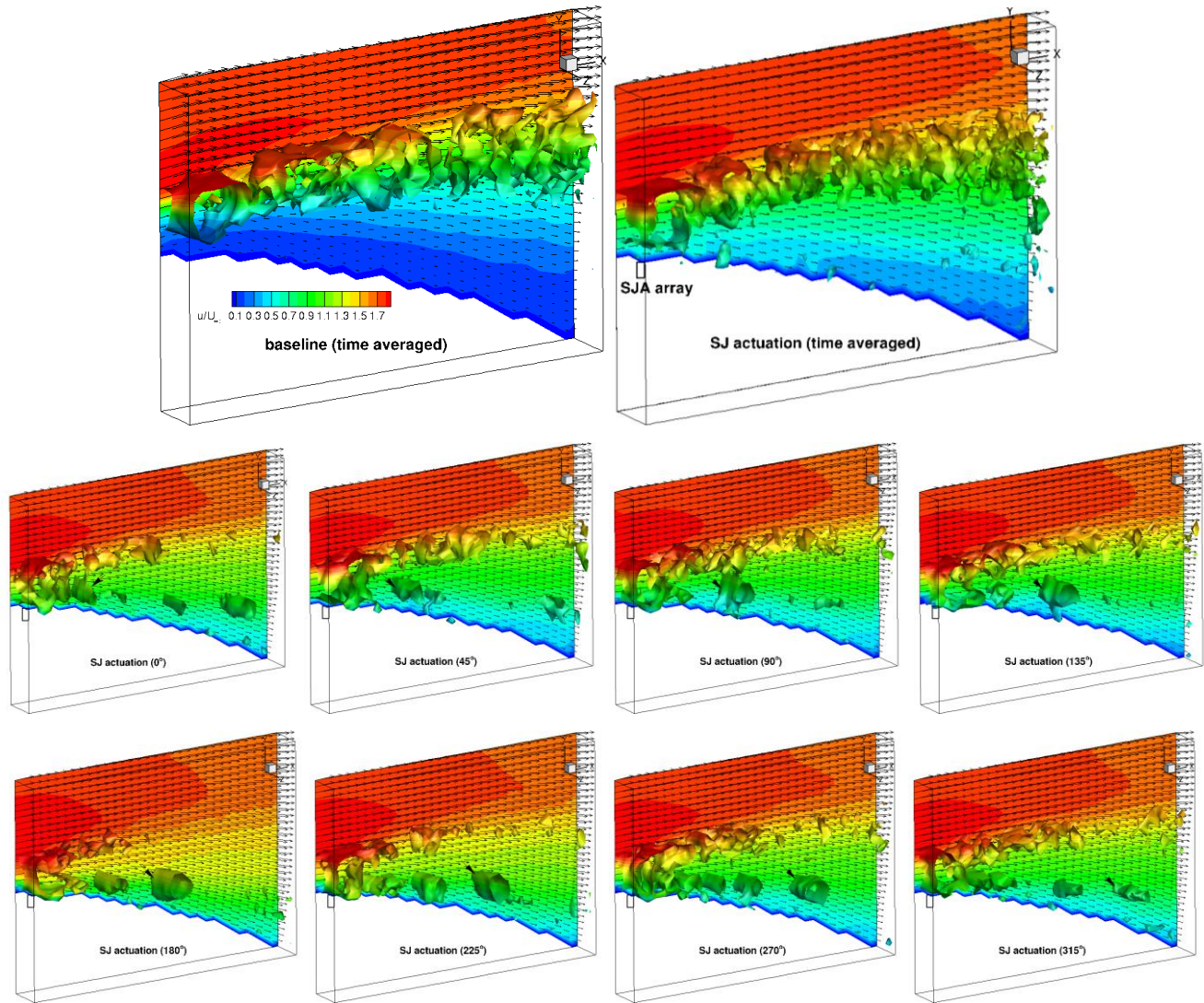

Fig. 3 Iso-surfaces of vortex structures colored by streamwise velocity for the time-averaged baseline case, time-averaged SJ actuation case and eight phase-averaged SJ actuation cases. The background shows a velocity vector field superimposed by streamwise velocity contours.

In addition to the findings from the time-averaged flow fields, the present study further reveals the flow fields at different actuation phase angles, as depicted in a sequence of smaller subplots in Fig. 3. The eight phase-averaged flow fields reveal that the interaction between the SJs and the boundary layer

flow results in the formation of near-wall spanwise vortices. The formation and propagation of a specific vortex is marked with an arrow in the subplots. It is found that, instead of being directly generated from the SJs, this near-wall vortex is shed from the separated shear layer, which however is induced by the SJs. It travels downstream with a speed of about 13 to 16 m/s, about the same speed as the free-stream flow over the suction surface of the wing model. During its downstream propagation, this vortex grows its size and strength successively up to the phase angle of 180º. Meanwhile, the largest improvement in the flow field also occurs at the phase angle of 180º as evident from the significant reduction in large-scale vortex structures in the shear layer zone as well as the substantial increase in the velocity of the near-wall flow as depicted by enlarged region of green and yellow color contours.

The largest improvement at the phase angle of 180º is also demonstrated in the alteration of near-wall velocities as shown in Fig. 4, where streamwise and cross-stream velocity profiles at four streamwise stations (x/c = 0.23, 0.29, 0.34 and 0.40) are presented for the time-averaged baseline case, time-averaged SJ-actuation case and four phase-locked SJ-actuation cases (phase angle 0°, 90°, 180° and 270°). Before switching on the SJ array, the baseline flow exhibits significant deficit of the streamwise velocity in the near-wall region, with the non-dimensional velocity reducing from about 1.8 in the free-stream to values less than 0.3. As shown in the first-row subplots, the height of the deficit region gradually increases as the flow develops downstream. Meanwhile, the flow also exhibits very weak downwash velocities (less than 0.1) in the near-wall region. These observations indicate the occurrence of a dominant flow phenomenon, i.e., flow separation, over the wing surface in the baseline case. Interestingly, even during flow separation very small but positive near-wall streamwise velocity is observed. This is because the presented velocity fields are time/phase averaged and during the experiments the "flapping" of the shear layer resulted in the onset of both separated and attached flows.

After actuating the SJ array, the near-wall streamwise velocity increases significantly as shown in the first-row subplots in Fig. 4. Among the four phase-locked cases, the highest and the lowest streamwise velocities near the wing surface occurs at phase angels 180° and 90°, respectively, at all the four stations. The velocity difference among different phases gradually reduces with the development of the flow. The mean increment in the wall-adjacent streamwise velocity is about 0.8 at Station 1 and gradually reduces at the following three downstream stations. As shown in the subfigures of the lower row in Fig. 4, the magnitude of negative cross-stream velocities increases significantly in the near-wall

8

region, indicating that a strong downwash flow is induced by the actuation of the SJ array. This induced downwash flow brings the outer high-momentum free-stream flow into the near-wall region and energizes the original retarding boundary layer flow. The profiles also confirm that the negative cross-stream velocity reaches its maximum at the phase angle 180° at all four stations.
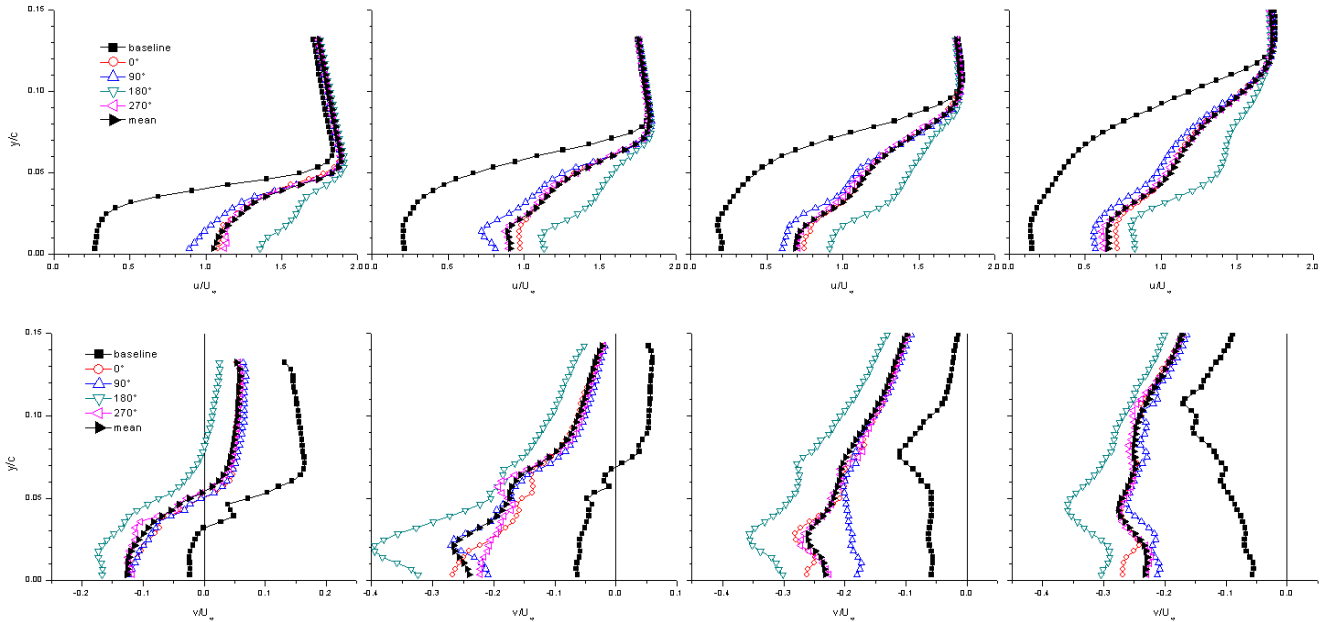

Fig. 4 Profiles of streamwise velocities (upper row) and cross-stream velocities (lower row) for the time-averaged baseline case and time- and phase-averaged SJ actuation cases at four streamwise stations. From left to right: x/c = 0.23, 0.29, 0.34 and 0.40. The vertical line in the lower row subfigures represents zero cross-stream velocity.

To unravel the reason why the SJ array exerts the largest influence at the phase angle of 180° as shown in Figs. 3 and 4, a hot-wire measurement was carried out in quiescent flow condition to determine the phase relation between the function generator signal and the actual SJ velocity. It is found that the phase angle 180° recorded by the function generator is only about 10° ahead of the instant corresponding to the SJ maximum blowing. This indicates that the highest blowing condition of the SJ array occurs near the phase angle of 180°. Therefore, the largest influence is observed at the phase angle of 180° as compared to rest of the phase angles.

Shape factor H, defined as the ratio of displacement thickness to momentum thickness, is a common factor used for assessing integral effect of flow control methods in boundary layer flows. The decrease of shape factor is a favorable indicator of enhanced ability in overcoming flow separation. The shape

factor for laminar boundary layers is generally higher than that for turbulent boundary layers and if it is higher than 3.5, laminar boundary layers are more prone to flow separation (Airiau et al. 2003). Figure 5 presents the chord-wise variation of shape factor for the time-averaged baseline case and the time-averaged SJ-actuation case. The measurement stations are taken uniformly at six streamwise locations ranging from $x/c = 0.23$ to 0.52. The shape factor of around 4 for the baseline case indicates the significant possibility of flow separation. After switching on the SJ array, the shape factor drastically reduces to below 2, confirming the effectiveness of the current SJ array in flow separation control.
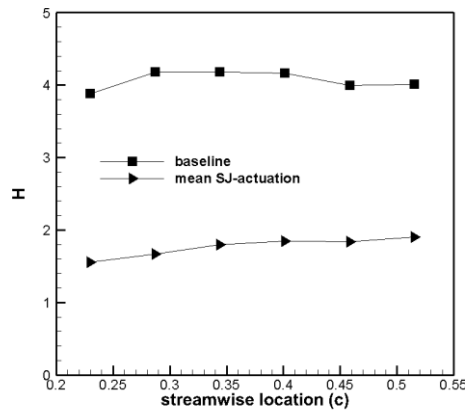

Fig. 5 Variation of shape factor along the chord for the baseline and time-averaged SJ-actuation cases

3.2. Analysis of energetic flow structures

Proper orthogonal decomposition (POD) analysis is a useful tool to determine the dominant energy carrying flow structures in an unsteady flow field and has been applied in many complex flow phenomena (Hilberg et al. 1994; Cazemier et al. 1998; Wu & Christensen 2010). The principle and equations of POD can be found in many places in literature and hence they are only briefly summarized below. In the present study, well-established snapshot POD was implemented on the Tomo-PIV measured 3D velocity fields above the wing surface. In POD, an unsteady velocity field $\boldsymbol{u}(\boldsymbol{x}, t)$ can be decomposed into the form of

$$\boldsymbol{u}(\boldsymbol{x},t) = \bar{\boldsymbol{u}}(\boldsymbol{x}) + \boldsymbol{u}'(\boldsymbol{x},t) = \bar{\boldsymbol{u}}(\boldsymbol{x}) + \sum_{n=1}^{N} q_n(t)\boldsymbol{\Phi}_n(\boldsymbol{x}) \tag{1}$$

where $\bar{u}(x)$ is the mean velocity field, $u'(x, t)$ the instantaneous fluctuating velocity field, $\Phi_n(x)$ deterministic spatial POD modes, $q_n(t)$ the temporal coefficient corresponding to the nth POD mode, and N the number of snapshots used in the calculation. The temporal coefficients $q_n(t)$ are obtained by solving an eigenvalue problem associated with $u'(x, t)$

$$\lambda_n q_n(t_i) = \sum_{j=1}^{N}\left(\sum_x u'(x, t_i) \cdot u'(x, t_j)\right)q_n(t_j) \tag{2}$$

where $()\cdot()$ represents the inner product of two vectors. For snapshot POD, t_i and t_j in Eq. (2) indicate the ith and jth snapshot, respectively, instead of actual time. The eigenvalues λ_n are real and positive, and form a decreasing and convergent series. The POD modes can then be calculated by

$$\Phi_n(x) = \frac{1}{\sqrt{\lambda_n N}}\sum_{i=1}^{N} u'(x, t_i)q_n(t_i) \tag{3}$$

Table 1 lists the fractional contributions of the first five POD modes to the total turbulent kinetic energy (TKE), $E_n = \lambda_n/\Sigma\lambda_n$, for both the baseline and SJ-actuation cases. It shows that, in both the cases, the first mode accounts for more than 70% of the energy and the energy contribution from any of the other modes is at least one order of magnitude less than that from the first mode. This indicates that the energy carried by the first mode's large-scale structures dominates the fluctuation of the flow field in both cases. This is quite different from POD analysis of other types of flow, e.g. turbulent boundary layer flows (Wu & Christensen 2010; Wu 2014), separated flow (Wu et al. 2015), and driven cavity flows (Cazemier et al. 1998), where the first mode is much less dominant and the TKE is more distributed into higher order modes.

Table 1: Fractional energy contributions of the first 5 POD modes for the baseline and SJ actuation cases

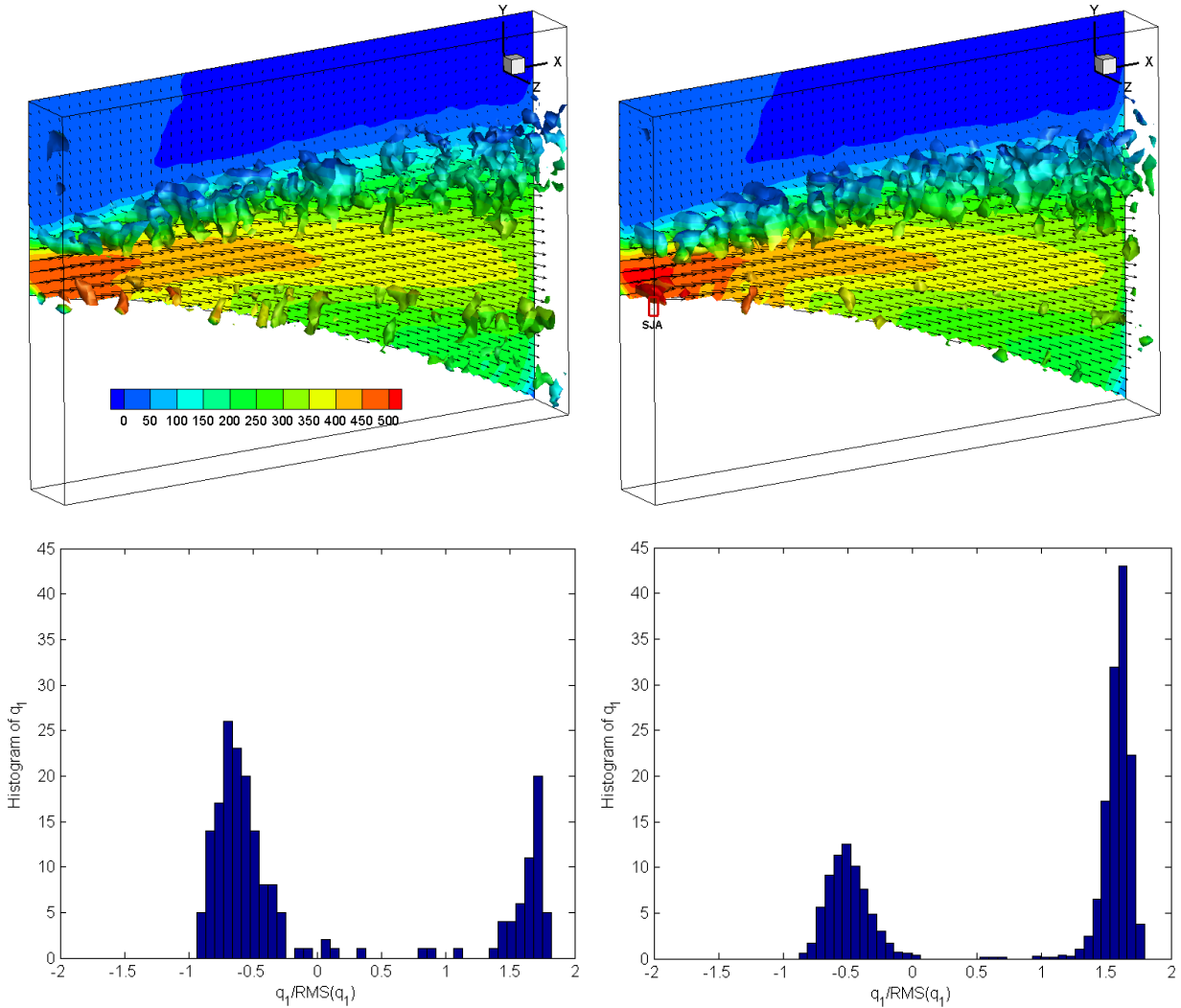| Mode #	1	2	3	4	5
Baseline	71.1%	2.4%	1.1%	0.8%	0.6%
SJ actuation	76.3%	1.6%	0.7%	0.6%	0.5%

Fig. 6 Upper row: iso-surfaces of vortex structures for the first POD mode for: (a) baseline case and (b) SJ actuation case. In the background, a vector field is superimposed by the streamwise eigen function contours. Lower row: distribution of q_1 values for (left) the baseline case and (right) SJ actuation case.

The vortex structures with a vector field plus streamwise component contours in the background for the first POD mode, Φ_1, are presented in Fig. 6 for both the baseline and SJ-actuation cases. Both cases share a very similar first mode, i.e., a 2D plane jet-like flow over the wing surface, with its upper edge consisting of a free shear layer and its lower edge attaching on the wing surface. Depending on the sign of its temporal coefficient, q_1, this mode represents either a momentum-injection flow (positive q_1) or an inverse flow (negative q_1) on top of the mean flow, as shown in the first row of Fig. 6. As a result, positive q_1 values correspond to snapshots with an attached flow, whereas negative q_1 values correspond to snapshots with a separated flow. Although the introduction of the SJ array seems to have

little effects on the first POD mode, it significantly increases the occurrence rate of positive q_1 values, or in other words, the possibility of flow attachment. In the present study, the ratio of the number of positive q_1 values to the total number of snapshots is about 30% for the baseline case and 65% for the SJ-actuation case, as clearly depicted in the bottom-row subplots of Fig. 6.

3.3. Turbulence analysis

As revealed in our previous work (Tang et al. 2014), the flow over the wing frequently switches back and forth between a separated flow and an attached flow, forming a "flapping" shear layer. The POD analysis in Section 3.2 further indicates that this type of large-scale flow pattern is the most fluctuation energy-carrying mode and the introduction of SJ array increases the occurrence rate of the attached flow. In addition to the switching between the separated flow and the attached flow, we also observed the fluctuations within the purely separated or attached flows. These fluctuations or "conditional" turbulence, may also be affected by the introduction of the SJ array. Hence in this section the effect of SJ array on one conditional turbulent quantity, i.e., the turbulence kinetic energy (TKE), is investigated.

To evaluate conditional turbulent quantities, a "conditional" mean velocity field is first calculated for one of the two types of flow patterns, i.e., either separated flows or attached flows. Corresponding conditional turbulent quantities for a specific type of flow patterns are then obtained based on the conditional mean velocity field. To obtain statistically meaningful data, the 12 streamwise-wall-normal data planes in each Tomo-PIV snapshot are treated as 12 individual measurements to increase the total number of samples. Note that although the calculation is conducted in a two-dimensional plane, the turbulent quantities are still three-dimensional, i.e., the TKE is calculated using the formula $k = (u'u'+v'v'+w'w')/2$.

Figure 7 shows the conditional TKE for the separated and attached flow cases, with and without SJ actuation. Comparison of the TKE contours as well as the mean flow streamlines in both the cases reveals that, while the introduction of the SJ array has little influence on the conditional TKE for the separated flows, it slightly reduces the thickness of the wall-attached layer carrying high TKE values for the attached flows.
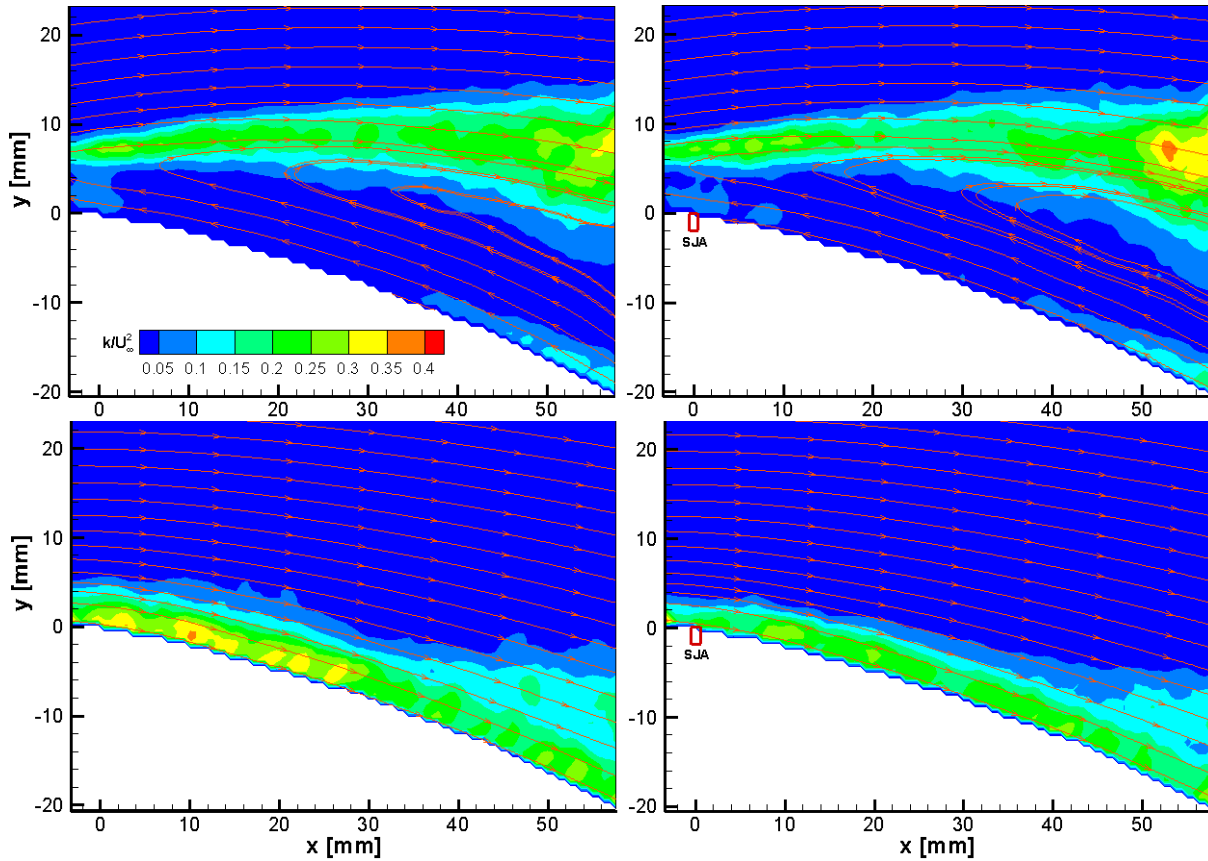
13

Fig. 7: Contours of conditional turbulent kinetic energy superimposed with streamlines of mean velocities for (left) the baseline case and (right) the time-averaged actuation case. Top: separated flows; bottom: attached flows.

4 Conclusions

This paper follows our previous work (Tang et al. 2014) to further demonstrate the effectiveness of a newly developed SJ array in flow separation control over a straight-wing model at an angle of attack of 19˚. Different from all existing SJ-based flow separation control, the present control is so mild that the controlled flow sometimes attaches to and sometimes separates from the wing surface. Tomo-PIV measurement results are presented, including time-averaged and phase-locked flow fields. It is observed that the introduction of the SJs induces spanwise vortices from the separated shear layer, which subsequently propagate downstream along the wing surface and interact with the boundary layer flow and exchanges the momentum. By comparing the streamwise and cross-stream velocities with and without actuating the SJ array, the control effect is found to reach its maximum at the nominal phase angle of 180°, which is close to the instant when the SJ array achieves its maximum blowing. In addition, a significant reduction of the shape factor from about 4 for the baseline case to below 2 for the

14

SJ controlled case is observed, confirming the effectiveness of the current SJ array in flow separation control. Subsequently, the POD analysis is implemented to extract the energetic flow structures from the PIV data. It is found that, no matter whether the SJ array is actuated or not, the first POD mode represents a 2D plane jet-like flow over the wing surface, which accounts for more than 70% of the total fluctuation energy. Although it seems that the present SJ array is not strong enough to change the first and dominant POD mode, the analysis of the coefficients of the first mode for all flow field snapshots reveals that the introduction of the SJ array significantly increases the possibility of flow attachment. Last, the snapshots of separated flows and attached flows are picked out separately to analyze the "conditional" turbulent quantities especially the TKE. It is found that while the introduction of the SJs has little influence on the conditional TKE for the separated flows, it slightly reduces the thickness of the wall-attached layer carrying high TKE values for the attached flows. Through this study, it can be concluded that although the control of the newly developed SJ array is mild, it is able to bring favorable change to a separated flow towards a fully attached flow.

Acknowledgements

References

Airiau C, Bottaro A, Walther S, Legendre D. A methodology for optimal laminar flow control: application to the damping of tollmien–schlichting waves in a boundary layer. *Physics of Fluids* 2003, 15: 1131–1145.

Amitay M, Glezer A. Role of actuation frequency in controlled flow reattachment over a stalled airfoil. *AIAA Journal* 2002, 40(2): 209–216.

Amitay M, Smith DR, Kibens V, Parekh DE, Glezer A. Aerodynamic flow control over an unconventional airfoil using synthetic jet actuators. *AIAA Journal* 2001, 39(3): 361–370.

Cazemier W, Verstappen RWCP, Veldman AEP. Proper orthogonal decomposition and low-dimensional models for driven cavity flows. *Physics of Fluids*, 1998, 10: 1685–1699.

Ciuryla M, Liu Y, Farnsworth J, Kwan C, Amitay M. Flight control using synthetic jets on a cessna 182 model, *Journal of Aircraft* 2007, 44: 642–653.

Crook A, Wood N. Measurements and visualisations of synthetic jets. AIAA Paper 2001–0145.

Elsinga G, Scarano F, Wieneke B, Oudheusden B. Tomographic particle image velocimetry, *Experiments in Fluids,* 2006, 41: 933–947.

Franck J, Colonius T. Effects of actuation frequency on flow control applied to a wall-mounted hump. *AIAA Journal,* 2012, 50: 1631-1634.

Glezer A, Amitay M. Synthetic jets. *Annual Review of Fluid Mechanics,* 2002, 34: 503-529.

Hilberg D, Lazik W, Fiedler H. The application of classical POD and snapshot POD in a turbulent shear layer with periodic structures. *Applied Scientific Research*, 1994, 53: 283–290.

Lee C, Hong G, Ha Q, Mallinson S. A piezoelectrically actuated micro synthetic jet for active flow control. *Sensors and Actuators A,* 2003, 108: 168–174.

Lee HM, Wu Y. An experimental study of stall delay on the blade of a horizontal-axis wind turbine using tomographic particle image velocimetry. *Journal of Wind Engineering and Industrial Aerodynamics*, 2013a, 123: 56-68.

Lee HM, Wu Y. Experimental study of rotational effect on stalling. *Chinese Physics Letters*, 2013b, 30: 064703.

Lee HM, Wu Y. A Tomo-PIV study of the effects of freestream turbulence on stall delay of the blade of a horizontal-axis wind turbine. *Wind Energy*, 2015, 18: 1185-1205.

Mccormick D. Boundary layer separation control with directed synthetic jets. AIAA Paper 2000–0519.

Melton L, Yao C, Seifert A. Application of excitation from multiple locations on a simplified high-lift system. AIAA Paper 2004–2324.

Scarano F, Poelma C. Three-dimensional vorticity patterns of cylinder wakes, *Experiments in Fluids*, 2009, 47: 69–83.

Smith BL, Glezer A. The formation and evolution of synthetic jets. *Physics of Fluids* 1998, 10(9): 2281.

Tang H, Salunkhe P, Zheng Y, Du J, Wu, Y. On the use of synthetic jet actuator arrays for active flow separation control. *Experimental Thermal and Fluid Science* 2014, 57: 1–10.

Wood J, Sahni O, Jansen K, Amitay M. Experimental and Numerical Investigation of Active Control of 3-D Flows, AIAA Paper 2009-4279.

Wu Y. A study of energetic large-scale structures in turbulent boundary layer, *Physics of Fluids*, 2014, 26(4): 045113.

Wu Y, Christensen KT. Spatial structure of a turbulent boundary layer with irregular surface roughness, *Journal of Fluid Mechanics* 2010, 655: 380–418.

Wu Y, Lee HM, Tang H. A study of the energetic turbulence structures during stall delay. *International Journal of Heat and Fluid Flow* 2015, 54: 183-195.

You D, Moin P. Active control of flow separation over an airfoil using synthetic jets. *Journal of Fluids and Structures* 2008, 24: 1349–1357.

Zhong S, Jabbal M, Tang H, Garcillan L, Guo F, Wood N, Warsop C. Towards the design of synthetic-jet actuators for full-scale flight conditions, *Flow, Turbulence and Combustion* 2007, 78(3-4): 283–307.

Zhong S, Zhang S. Further examination of the mechanism of round synthetic jets in delaying turbulent flow separation. *Flow, Turbulence and Combustion* 2013, 91(1): 177–208.

Zhou J, Adrian RJ, Balachandar S, Kendall TM. Mechanisms for generating coherent packets of hairpin vortices in channel flow. *Journal of Fluid Mechanics* 1999, 387: 353–396.